Research Article

Petrogenesis of Late Early Cretaceous high-silica granites from the Bangong–Nujiang suture zone, Central Tibet

Wan-Long Hu [a,b], Qiang Wang [a,b,c,*], Jin-Hui Yang [d], Gong-Jian Tang [a,c], Lin Ma [a], Zong-Yong Yang [a,e], Yue Qi [a], Peng Sun [a]

[a] State Key Laboratory of Isotope Geochemistry, Guangzhou Institute of Geochemistry, Chinese Academy of Sciences, Guangzhou 510640, China
[b] College of Earth and Planetary Sciences, University of Chinese Academy of Sciences, Beijing 100049, China
[c] CAS Center for Excellence in Tibetan Plateau Earth Sciences, Beijing 100101, China
[d] Institute of Geology and Geophysics, Chinese Academy of Sciences, Beijing 100029, China
[e] State Key Laboratory of Ore Deposit Geochemistry, Institute of Geochemistry, Chinese Academy of Sciences, Guiyang 550002, China

ARTICLE INFO

ABSTRACT

High-silica granites are common in collisional orogenic belts. However, the petrogenesis of such granites and the geodynamic processes associated with their emplacement are debated. In this study, we present zircon U–Pb ages and Hf isotopes, and whole-rock geochemical and Sr–Nd isotopic compositions for biotite granites from the Jiang Co area, in the Bangong–Nujiang suture zone, central Tibet. Zircon U–Pb dating reveals that the Jiang Co granites were emplaced during the late Early Cretaceous (ca.114 Ma). These granites are characterized by high and variable SiO_2 (69.7–78.2 wt%) and K_2O (4.7–8.4 wt%), and low MgO (0.09–1.25 wt%) and P_2O_5 (< 0.1 wt%) contents. The samples are enriched in Rb, Th, U, and Pb, and depleted in Ba, Nb, Ta, Sr, Ti, and Eu. These geochemical features suggest that the Jiang Co granites underwent extensive fractional crystallization. The high and variable initial $^{87}Sr/^{86}Sr$ (0.7066 to 0.7095) ratios and consistent $\varepsilon_{Nd}(t)$ (−8.2 to −9.2) values, along with T_{Nd}^{2DM} ages of 1.66 to 1.58 Ga, and negative to positive zircon $\varepsilon_{Hf}(t)$ (−7.5 to +1.8) values, imply that these granites were formed by partial melting of the mature ancient crustal materials with minor involvement of mantle materials. Along with contemporaneous magmatic activity, we suggest that the Jiang Co granites were mainly generated by crustal melting in a post-collisional setting resulting from slab breakoff after the Lhasa–Qiangtang collision, and subsequently underwent a high degree fractional crystallization.

© 2020 Elsevier B.V. All rights reserved.

1. Introduction

High-silica granites occur in many tectonic environments, from extensional regimes and orogenic margins to continental collision zones (Bagdonas et al., 2016; Frost et al., 2016; Gao et al., 2017; Ji et al., 2020; Jung et al., 2012; Ma et al., 2017; Wu et al., 2020). These rocks, which have high silica (SiO_2 > 70 wt%) and potassium contents, are important carrier of incompatible elements and commonly associated with the eruption of rhyolite (Bachmann and Bergantz, 2008; Lee and Morton, 2015), thus, understanding their formation is important for studying the evolution of the continental crust (Glazner et al., 2008; Lee and Morton, 2015). Petrogenetic models for the formation of high-silica magma include fractional crystallization (Ji et al., 2020; Lee and Morton, 2015; Putirka et al., 2014; Wu et al., 2017; Zhang et al., 2018) and low-degree partial melting of granodiorites (Glazner et al., 2008)

or partial melting of metasedimentary rocks (Frost et al., 2016; Nabelek and Liu, 2004). However, many studies suggested that high-silica magmas cannot be formed by fractionation due to its high viscosity (Glazner, 2014; Petford, 2003). On the contrary, others argued that hydrous high-silica magmas have relatively low viscosity, and this makes significant fractionation possibly occur (Ji et al., 2020; Lee et al., 2015; Wu et al., 2017). Therefore, whether high-silica magmas could be formed by significant fractionation remains highly controversial and requires further studies (Glazner 2014; Lee et al., 2015; Searle et al., 2009; Wu et al., 2017).

The Bangong–Nujiang suture zone (BNSZ), which is located between the Qiangtang terrane to the north and the Lhasa terrane to the south, records the subduction history of the Bangong–Nujiang Tethys Ocean and subsequent Lhasa–Qiangtang collision (Guynn et al., 2006; Kapp et al. 2007; Yin and Harrison, 2000; Zhu et al., 2013, 2016). Voluminous Mesozoic igneous rocks are widely distributed along the BNSZ, central Tibet (He et al., 2019; Hu et al. 2017, 2019; Liu et al., 2017; Yang et al., 2019; Zhu et al., 2016 and references therein). The igneous rocks provide important evidence for double subduction of Bangong–Nujiang Tethys oceanic lithosphere and continental collision (Zhu et al., 2016 and

references therein). High-silica granites have recently been recognized near the BNSZ, including the Chuburi granites in the southern Qiangtang subterrane and the Gajin granites in the Lhasa terrane (Fig. 1b; He et al., 2019; Yang et al., 2019). Theses granites, which have silica contents of 71–78 wt% SiO₂, are not associated with intermediate and mafic rocks. Despite their petrologic similarities, the petrogenetic processes for coeval high-silica granites remain uncertain and require more detailed research (He et al., 2019; Yang et al., 2019; Zhu et al., 2016).

In this paper, we report whole-rock major- and trace-element and Sr–Nd isotopic compositions, and zircon U–Pb ages and Hf isotopic data from the Jiang Co high-silica granites, which were found within the middle-eastern segments of the BNSZ, central Tibet. These results are used to discuss the petrogenesis of high-silica granites, and better understand the characteristics and generation of the magmatism associated with a collisional orogenic event.

2. Geological setting and petrographic characteristics

The Tibetan Plateau consists of a tectonic collage of different crustal blocks. From north to south, the main continental terranes are the Songpan–Ganzi, Qiangtang, Lhasa, and Himalaya. These terranes are separated by the Jinsha suture zone (JSSZ), Bangong–Nujiang suture zone (BNSZ), and Indus–Yarlung Zangbo suture zone (IYZSZ), respectively (Yin and Harrison, 2000; Fig. 1a). In central Tibet, the BNSZ extends east–west for more than 2000 km through the Bangong Co,

Gerze, Dongqiao, Dengqen, and Jiayuqiao areas, and into Burma, Thailand, and Malaysia; it marks the boundary between the Qiangtang terrane to the north and the Lhasa terrane to the south (Fig. 1b; Yin and Harrison, 2000; Zhu et al., 2016). It can be generally subdivided into the western (Bangong Co–Gaize), the middle (Dongqiao–Amdo), and the eastern (Dengqen–Nujiang) segments (e.g., Pan et al., 2012; Yin and Harrison, 2000). This suture zone consists of scattered ophiolitic fragments, radiolarian cherts, oceanic island (or seamount), arc volcanic-magmatic rocks, flysch-like deposits, and accretionary complexes (Fig 1b; e.g., Fan et al., 2015; Li et al. 2018, 2019; Liu et al., 2016; Wang et al., 2016; Zhu et al., 2016). In southern Qiangtang subterrane, to the north of the BNSZ, Early Paleozoic gneissic granites (~480–465 Ma) were emplaced into Cambrian metasedimentary rocks in the Duguer and Bengsong Co areas, and are considered to represent the crystalline basement (Dan et al., 2020). The subterrane was widely covered by the Carboniferous, Permian and Jurassic sedimentary sequences, which consist of sandstone, mudstone, and limestone (Li et al., 2017; Zhu et al., 2013). Late Mesozoic magmatic rocks are widely distributed in the southern Qiangtang subterrane (Fig. 1b). These rocks are dominated by intermediate–felsic magmatic rocks, and their geochronological data indicate that they were emplaced between 183 and 73 Ma (e.g., Guynn et al., 2006; Hao et al., 2016, 2019; He et al., 2019; Li et al., 2014, 2018, 2019; Liu et al., 2017; Zhang et al., 2012; Zhu et al., 2016). To the south of the BNSZ, the northern Lhasa subterrane mainly consists of juvenile crust (Zhu et al., 2011, 2013), and the
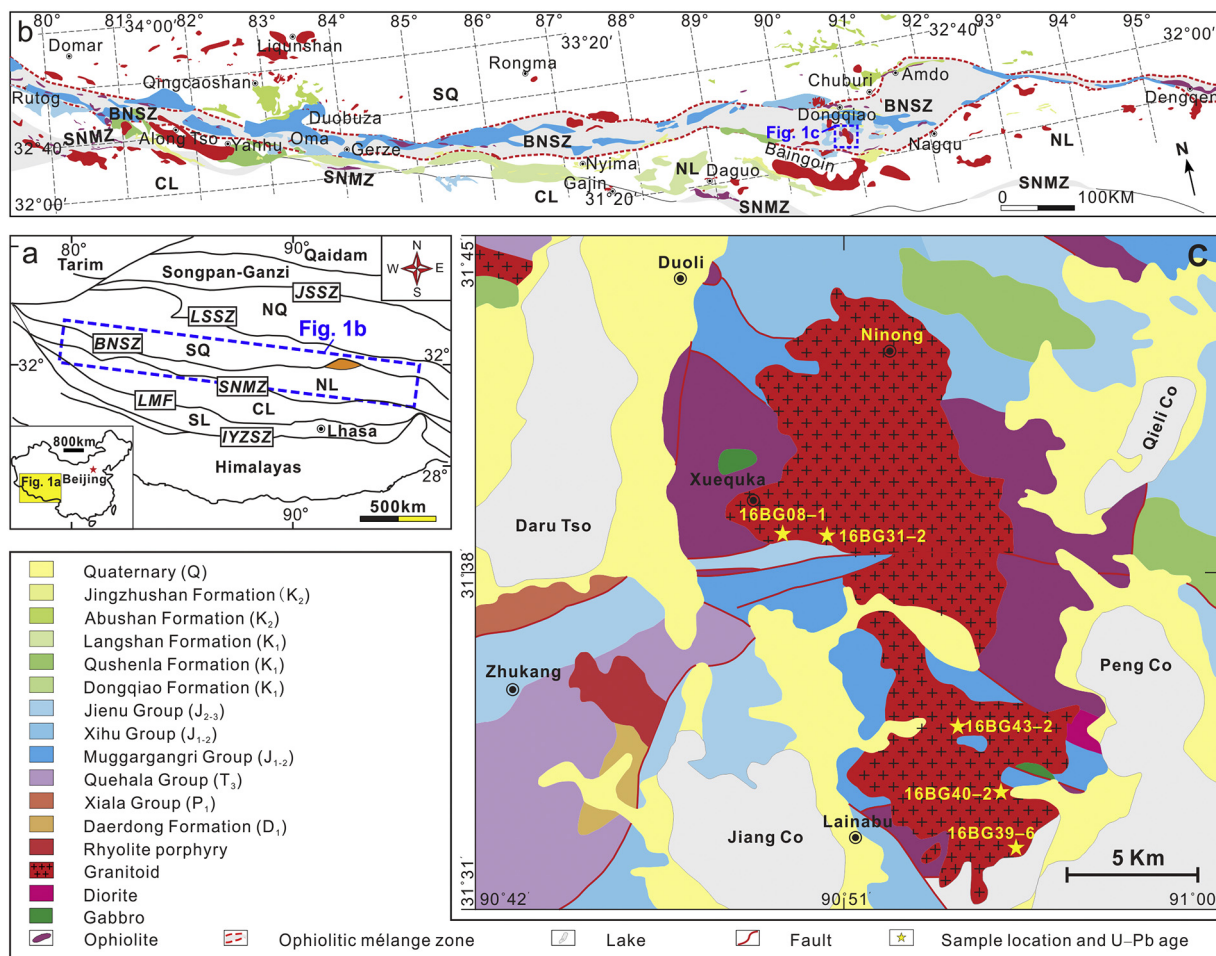

Fig. 1. (a) Sketch geological map of Tibet. JSSZ = Jinsha suture zone; NQ = Northern Qiangtang subterrane; LSSZ = Longmu Co–Shuanghu suture zone; SQ = Southern Qiangtang subterrane; BNSZ = Bangong–Nujiang suture zone; NL = Northern Lhasa subterrane; SNMZ = Shiquan River–Nam Tso Mélange zone; CL = Central Lhasa subterrane; LMF = Luobadui–Milashan Fault; SL = Southern Lhasa subterrane; IYZSZ = Indus–Yarlung Zangbo suture zone. (b) Geological map of the Bangong–Nujiang suture zone (modified after Zhu et al. 2016). (c) Geological map of the Jiang Co area.

subterrane is covered by the Middle Triassic-Cretaceous sedimentary rocks (Zhu et al. 2013, 2016). The magmatic rocks are exposed in the northern Lhasa subterrane, including Along Tso Batholith, Gajin plutons, Baingoin Batholith, and extensive Early Cretaceous volcanic rocks (Fig. 1b; e.g., Sui et al., 2013; Yang et al., 2019; Zhu et al. 2013, 2016).

The Amdo terrane is located within the middle-eastern segments of the BNSZ between the southern Qiangtang subterrane to the north and the northern Lhasa subterrane to the south (Fig. 1b). The microcontinent consists mainly of strongly foliated gneisses, metasedimentary rocks, and undeformed granitoids (Guynn et al. 2006, 2012; Zhang et al., 2014; Zhu et al. 2013). The Amdo orthogneisses show a bimodal distribution of crystallization ages of 915–840 Ma and 530–470 Ma, providing direct evidence for the presence of a Neoproterozoic—early Paleozoic basement in the Amdo terrane (Guynn et al. 2006, 2012). The metasedimentary rocks consist of marble, schist, phyllite, and quartzite, and were likely deposited in a passive continental margin setting (Guynn et al., 2012). The undeformed granitoids (185–175 Ma) intruded the Amdo basement (Guynn et al., 2006), and their zircon Hf isotopic compositions revealed the presence of a Meso- to Paleo-Proterozoic basement at the subsurface (Zhu et al., 2011).

The Baingoin–Zigetang Co areas are also located in the middle-eastern segments of the BNSZ and adjacent to the Amdo terrane (Fig. 1b). The outcrops in this area consist mostly of Paleozoic sedimentary strata, Jurassic rock units (sandstones with interstratified volcanic rocks, flysch sediments, and limestones), Lower Cretaceous volcano-sedimentary units (volcanic rocks and conglomerates), granitoids, ophiolitic fragments and Quaternary deposits (Fig. 1c). The ophiolitic fragments from Baingoin–Zigetang Co areas were produced at the Early Jurassic (~188 Ma; Liu et al., 2016) and Late Jurassic (~147 Ma; Zhong et al., 2017), respectively. All these ophiolites were formed in a fore-arc oceanic setting, indicate that the BNTO, in particular its middle-eastern segments, was not closed until the Late Jurassic (Liu et al., 2016; Wang et al., 2016; Zhong et al., 2017). The volcanic rocks can be divided into two major stages, including the Jurassic (185–150 Ma) and the Early Cretaceous (126–100 Ma). Small volumes of Early–Middle Jurassic volcanic rocks are exposed within the BNSZ, and their generation is attributed to subduction of the Bangong–Nujiang Oceanic lithosphere (Tang et al., 2019; Zeng et al., 2016). The Early Cretaceous volcanic rocks unconformably overlie the Jurassic rock units, and are widely exposed in the BNSZ and the northern part of the Lhasa terrane (e.g., the Qushenla and Duoni Formations, Hu et al., 2017; Zhu et al., 2016). The Cretaceous granitoids were also widely emplaced in this area, however, little is known about the petrogenesis of these rocks (Zhu et al., 2016).

The Jiang Co granites, located ~15 km north of Baila town, make up one of the largest batholiths in the BNSZ. These granites intruded into Jurassic sedimentary rocks, the Early–Middle Jurassic Muggargangri Group, and the Jiang Co ophiolites (Figs. 1c and 2a–c). The Jiang Co pluton shows medium- to coarse- grained, fine-grained granular, and porphyritic textures. The medium- to coarse- grained granites consist of quartz (25–30 vol%), alkali feldspar (20–30 vol%), plagioclase (25–30 vol%), biotite (0–10 vol%), as well as minor accessory minerals of zircon, apatite, magnetite, and titanite (Fig. 2d). The fine-grained granular granites are composed of quartz (30–35 vol%), alkali feldspar (30–35 vol%), plagioclase (20–25 vol.%), biotite (~5 vol%), and accessory minerals include zircon, apatite, titanite, magnetite, and ilmenite (Fig. 2e). The porphyritic granites contain ~35 vol% phenocrysts and ~65 vol % groundmass. The phenocrysts include anhedral quartz (~25 vol %), plagioclase (~5 vol%), and biotite (~5 vol%). The groundmass also consists of mainly quartz, alkali feldspar, plagioclase, and biotite as well as minor accessory minerals (Fig. 2f). Feldspars from some samples are variably affected by sericitization and epidotization (Fig. 2d–f).

3. Analytical methods

3.1. Zircon U–Pb dating and Lu–Hf isotopic analyses

Laser ablation (LA)–ICP–MS zircon U–Pb analyses were performed using an Agilent 7500a ICP–MS with an attached 193 nm excimer ArF laser-ablation system (GeoLas Plus) at the Institute of Geology and Geophysics, Chinese Academy of Sciences (IGG CAS). A more detailed description of the analytical technique is provided by Xie et al. (2008). The analyses were conducted with a spot diameter of 35 μm with a typical ablation time of approximately 30 s for 200 cycles of each measurement, an 8 Hz repetition rate, and a laser power of 100 mJ/pulse. Common Pb was corrected according to the method proposed by Andersen, (2002). The secondary standard zircon GJ–1 was analyzed as unknown samples to monitor the reliability of the whole procedure. Twelve measurements on zircon GJ–1 yielded a concordia age of 607.2 ± 1.3 Ma (Table S5), which is within error of the recommended value of 608.5 ± 0.4 Ma (Jackson et al., 2004). The isotopic ratios and element concentrations of zircon were calculated with GLITTER 4.4. The weighted mean U–Pb ages and Concordia plots were processed using the Isoplot/Ex v. 3.0 program (Ludwig, 2003).

In situ zircon Lu–Hf isotopic analyses were carried out on a Neptune Plus multi-collector ICP-MS equipped with a RESOlution M-50 193 nm laser-ablation system at the State Key Laboratory of Isotope Geochemistry, Guangzhou Institute of Geochemistry, Chinese Academy of Sciences (SKLaBIG GIG CAS). Lu–Hf isotopic analyses were conducted on the same zircon grains that were previously analyzed for U–Pb isotopes, with ablation pits of 45 μm in diameter, ablation time of 30s, repetition rate of 6 Hz, and laser beam energy density of 4 J/cm^2. The detailed analytical procedures were similar to those described by Zhang et al. (2015). Measured ^{176}Hf/^{177}Hf ratios were normalized to ^{179}Hf/^{177}Hf = 0.7325. The measurements of the Penglai zircon standard during the course of this study yielded a weighted mean of ^{176}Hf/^{177}Hf = 0.282905 ± 0.000024 (n = 24, 2SD), which is consistent within errors with the reported value in Li et al. (2010).

3.2. Whole-rock element analyses

Rock samples were crushed by a jaw crusher and then powdered to ~200 mesh in an agate mill, and the resulting powder was used for geochemical analyses. Major element oxides were analyzed on fused glass beads using a Rigaku RIX 2000 X-ray fluorescence spectrometer at the SKLaBIG GIG CAS. The analytical procedures were the same as those described by Li et al. (2000). Glass discs were made by melting dehydrated sample powders. Calibration lines used in quantification were produced by bivariate regression of data from 36 reference materials encompassing a wide range of silicate compositions (Li et al., 2005), and analytical uncertainties are between 1% and 5%.

Trace elements were analyzed by inductively coupled plasma mass spectrometry (ICP-MS), using a Perkin-Elmer Sciex ELAN 6000 instrument at the SKLaBIG GIG CAS. Analytical procedures are the same as those described by Li et al., (2002). An internal standard solution containing the single element Rh was used to monitor signal drift during counting. The trace element compositions of reference materials (W–2a, BHVO–2, AGV–2, GSR–1, GSR–2 and GSR–3) and replicate sample 16BG42–3R are given in Table S6. Repeated runs give <3% RSD (relative standard deviation) for most elements of reference materials for ICP-MS analyses.

3.3. Whole-rock Sr–Nd isotopic analyses

The Sr–Nd isotopic compositions of selected samples were determined using a Neptune multicollector–ICP–MS (MC–ICP–MS) at the SKLaBIG GIG CAS. Analytical procedures are similar to those described in Li et al. (2004). Sr and REE were separated using cation columns, and Nd fractions were further separated by HDEHP-coated Kef columns.
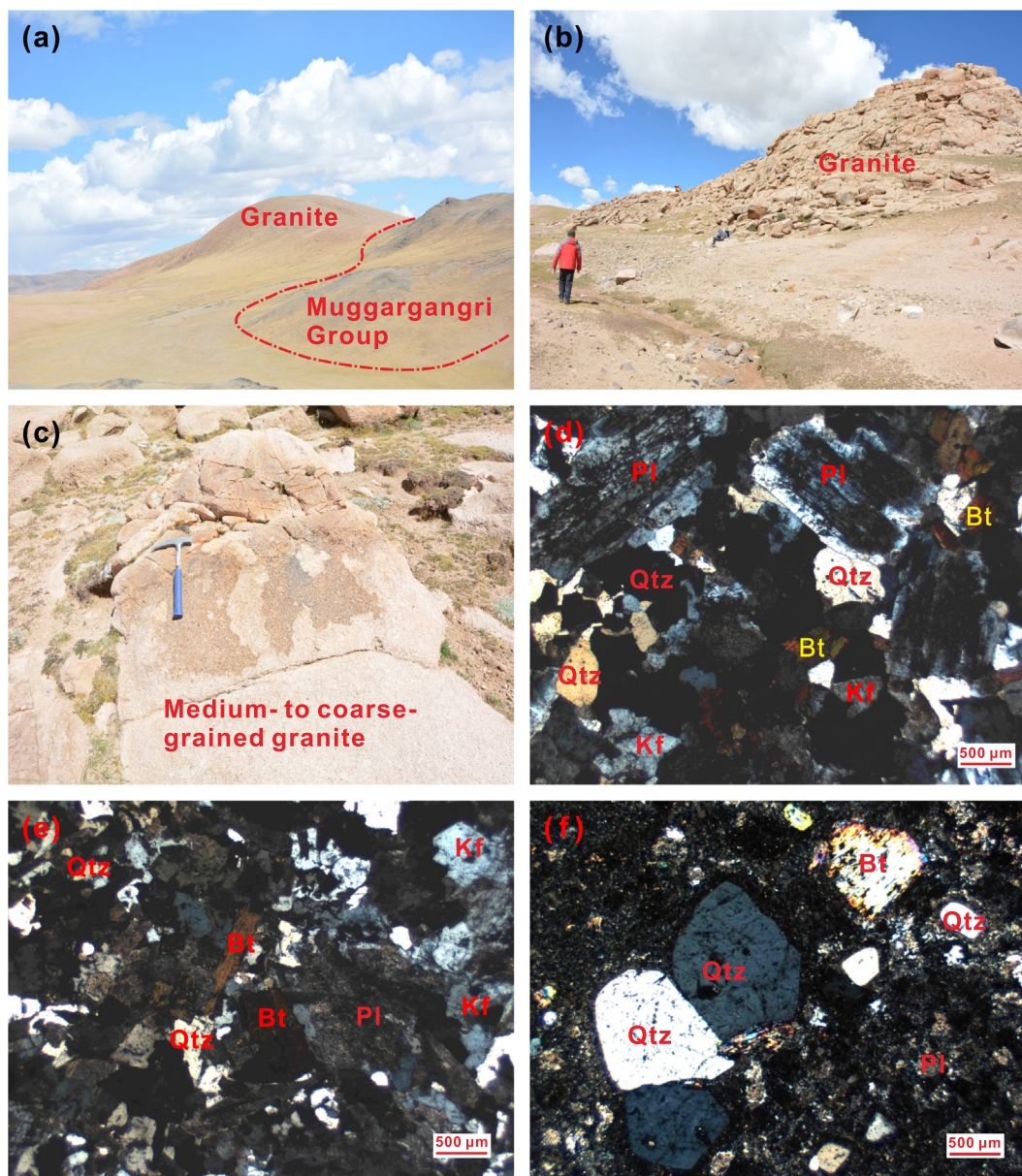
Fig. 2. (a)–(c) Field photographs of Jiang Co granites; (d)–(f) Photomicrographs showing the medium-grained granitic, fine-grained granular, and porphyritic textures of the Jiang Co granites, respectively. Abbreviations: Qtz = quartz, Kf = K-feldspar, Pl = plagioclase, Bt = biotite.

The $^{87}Sr/^{86}Sr$ ratio of the NBS 987 standard and $^{143}Nd/^{144}Nd$ ratio of the Shin Etsu JNdi–1 standard were 0.710270 ± 0.000022 (n = 7, 2SD) and 0.512116 ± 0.00008 (n = 7, 2SD), respectively. All measured $^{143}Nd/^{144}Nd$ and $^{87}Sr/^{86}Sr$ ratios were normalized to $^{146}Nd/^{144}Nd = 0.7219$ and $^{86}Sr/^{88}Sr = 0.1194$, respectively.

4. Results

4.1. Zircon U–Pb ages

Five samples were selected for zircon U–Pb dating, including samples 16BG08–1, 16BG31–2, 16BG39–6, 16BG40–2 and 16BG43–2. Zircons from the five samples are mostly transparent and colorless under the optical microscope, and have crystal lengths of ~80–200 μm and length/width ratios from 1:1 to 3:1. Most of the zircon grains show concentric oscillatory zoning in cathodoluminescence (CL) images (Fig. 3a), and have high Th/U ratios (0.29–2.15), indicating a magmatic

origin (Hoskin and Schaltegger, 2003). U–Pb Concordia diagrams of the analyzed zircon grains are shown in Fig. 3b–f, and U–Pb age data are presented in Table S1.

Sample 16BG40–2 is a medium- to coarse- grained granite, and zircon grains from this sample exhibit high and variable Th (180–513 ppm) and U (202–470 ppm) contents, with moderate to high Th/U (0.68–1.13) ratios. The zircon grains yield a mean $^{206}Pb/^{238}U$ ages of 114.7 ± 0.9 Ma (Fig. 3e). Samples 16BG08–1 and 16BG39–6 are fine-grained granular granites and have mean $^{206}Pb/^{238}U$ ages of 115.0 ± 0.8 Ma (Fig. 3b) and 114.4 ± 0.8 Ma (Fig. 3d), respectively. The analyzed zircon grains from samples 16BG08–1 and 16BG39–6 have variable Th (244–759 ppm and 405–5,947 ppm, respectively) and U (264–732 ppm and 524–2,763 ppm, respectively) concentrations, and Th/U ratios of 0.68–1.34 and 0.29–2.15, respectively. In addition, sample 16BG39–6 contains inherited zircon grains with variable dates (1042–158 Ma). Samples 16BG31–2 and 16BG43–2 are porphyritic granites. The zircons from samples 16BG31–2 and 16BG43–2 have
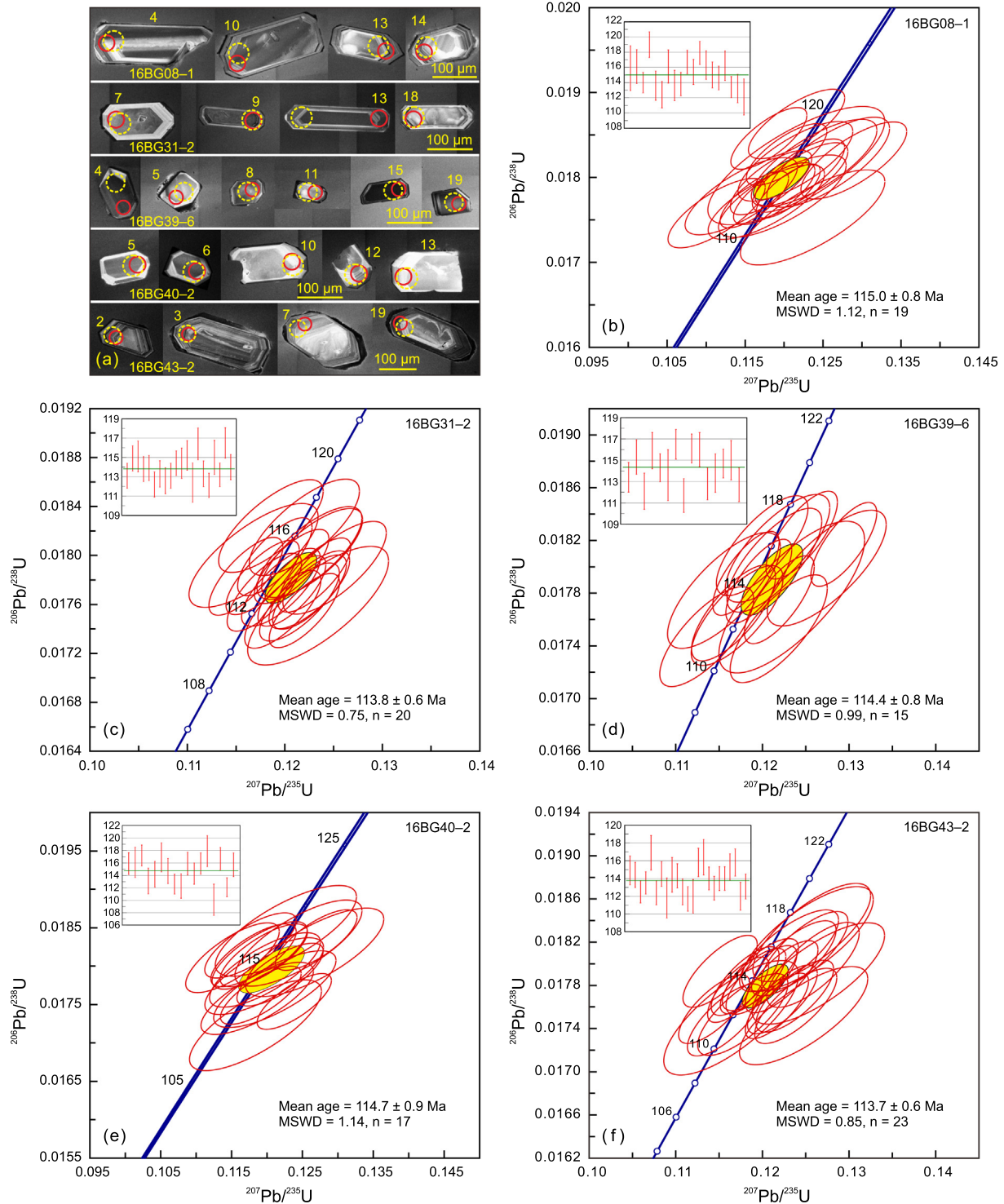
Fig. 3. (a) Representative cathodoluminescence (CL) images of zircon grains. Red solid circles delineate the spots analyzed for U–Pb dating; yellow dashed circles mark the spots analyzed for Hf isotopes. (b–f) LA–ICP–MS zircon U–Pb concordia diagrams for the Jiang Co granites.

high and variable Th (239–1459 ppm and 203–828 ppm, respectively) and U (318–1161 ppm and 240–921 ppm, respectively) contents, with Th/U ratios of 0.51–1.26 and 0.46–1.35, respectively. They yield weighted mean $^{206}Pb/^{238}U$ ages of 113.8 ± 0.6 Ma (Fig. 3c) and 113.7 ± 0.6 Ma (Fig. 3f), respectively. In summary, the zircon U–Pb age data indicate that the granites in the Jiang Co area were all formed at ca. 114 Ma.

4.2. Whole-rock major and trace element compositions

Whole-rock major and trace elements analytical results are listed in Table S2. The Jiang Co granites are characterized by high and variable SiO_2 (69.7–78.2 wt%) contents, similar to the high-silica granites from adjacent areas (e.g., He et al., 2019; Yang et al. 2019). The samples also have high Al_2O_3 (11.3–14.6 wt%), K_2O (4.7–8.4 wt%) and total alkali

(K_2O + Na_2O = 7.8–9.2 wt%) contents, and all samples have K_2O/Na_2O (> 1) ratios, and low TiO_2 (0.08–0.42 wt%), CaO (0.07–2.43 wt%), and MgO (0.09–1.25 wt%) contents. On the TAS diagram (Fig. 4a), all of the samples fall within the subalkaline granite field, and most of them plot in the field of high-K calc-alkaline field on a K_2O—SiO_2 diagram (Fig. 4b), except for four samples (16BG31−1, 16BG31−2, 16BG43−1, and 16BG43−2). The Jiang Co granites have a wide range of A/CNK (A/CNK = molecular Al_2O_3/(CaO + Na_2O + K_2O) = 1.0–1.4) values, indicating that these samples are peraluminous to strongly peraluminous rocks (Fig. 4c). On Harker diagrams, the studied samples show a general trend of decreasing TiO_2, Al_2O_3, Fe_2O_3, MgO, CaO and P_2O_5 with increasing SiO_2 (Fig. 5).

The samples of these granites have relatively high concentrations of total rare earth elements (ΣREEs; 133–257 ppm). Chondrite-normalized REE patterns (Fig. 6a) show relative enrichment of light rare earth elements (LREEs), with a remarkably negative Eu anomaly (Eu/Eu* = Eu_N/[Sm_N × Gd_N]$^{1/2}$ = 0.1–0.6) and variable $(La/Yb)_N$ (3.7–18.9) ratios. In the primitive mantle-normalized spider diagrams (Fig. 6b), the Jiang Co granites are enriched in large ion lithophile elements (LILEs; e.g., Rb, Th, K, and U) and Pb, depleted high field strength elements (HFSEs; e.g., Nb, Ta, Ti, P, and Zr), and have marked negative Sr and Ba anomalies.

4.3. Whole-rock Sr–Nd isotopic compositions

The Sr–Nd isotopic compositions are presented in Table S3. Zircon U–Pb weighted mean ages from this study were used to calculate the initial Sr–Nd isotopic compositions. Several samples have high $^{87}Rb/^{86}Sr$ (> 15) ratios that the initial $^{87}Sr/^{86}Sr$ ratios cannot be used to infer their petrogenesis (Wu et al., 2002). Other samples with low $^{87}Rb/^{86}Sr$ (< 6) ratios have high and variable initial $^{87}Sr/^{86}Sr$ ratios of 0.7066–0.7095 (Fig. 7a). They have negative and relatively uniform $\varepsilon_{Nd}(t)$ (−9.2 to −8.2) values, corresponding to two-stage Nd model ages (T_{Nd}^{2DM}) ranging from 1.66 to 1.58 Ga (Fig. 7a and Table S3).

4.4. Zircon Hf isotopes

In situ LA–MC–ICP–MS Lu–Hf isotopic analyses were conducted on the zircon grains that were previously analyzed for U–Pb isotopes. Zircon Hf isotopic data are presented in Table S4. The $\varepsilon_{Hf}(t)$ values and two-stage model ages were calculated using every zircon U–Pb date of each sample. Zircon grains from sample 16BG08–1 yield initial $^{176}Hf/^{177}Hf$ values of 0.282488−0.282599 and negative $\varepsilon_{Hf}(t)$ values in the range of −7.5 to −3.6, corresponding to two-stage Hf model (T_{Hf}^{2DM}) ages of 1.65–1.40 Ga (Fig. 8a). Zircon grains from sample 16BG31–2 yield initial $^{176}Hf/^{177}Hf$ values of 0.282492–0.282624 and $\varepsilon_{Hf}(t)$ values from −7.4 to −2.7, corresponding to the T_{Hf}^{2DM} ages varying of 1.64–1.35 Ga (Fig. 8b). Zircon grains from sample 16BG39–6 yield initial $^{176}Hf/^{177}Hf$ values of 0.282497–0.282752 and variable $\varepsilon_{Hf}(t)$ values ranging from −7.2 to 1.8, with the corresponding T_{Hf}^{2DM} ages of 1.63–1.06 Ga (Fig. 8c). Zircon grains from sample 16BG40–2 yield initial $^{176}Hf/^{177}Hf$ values of 0.282517–0.282604 and $\varepsilon_{Hf}(t)$ values of −6.5 to −3.4, with the corresponding T_{Hf}^{2DM} ages varying from 1.59–1.39 Ga (Fig. 8d). Zircon grains from sample 16BG43–2 yield initial $^{176}Hf/^{177}Hf$
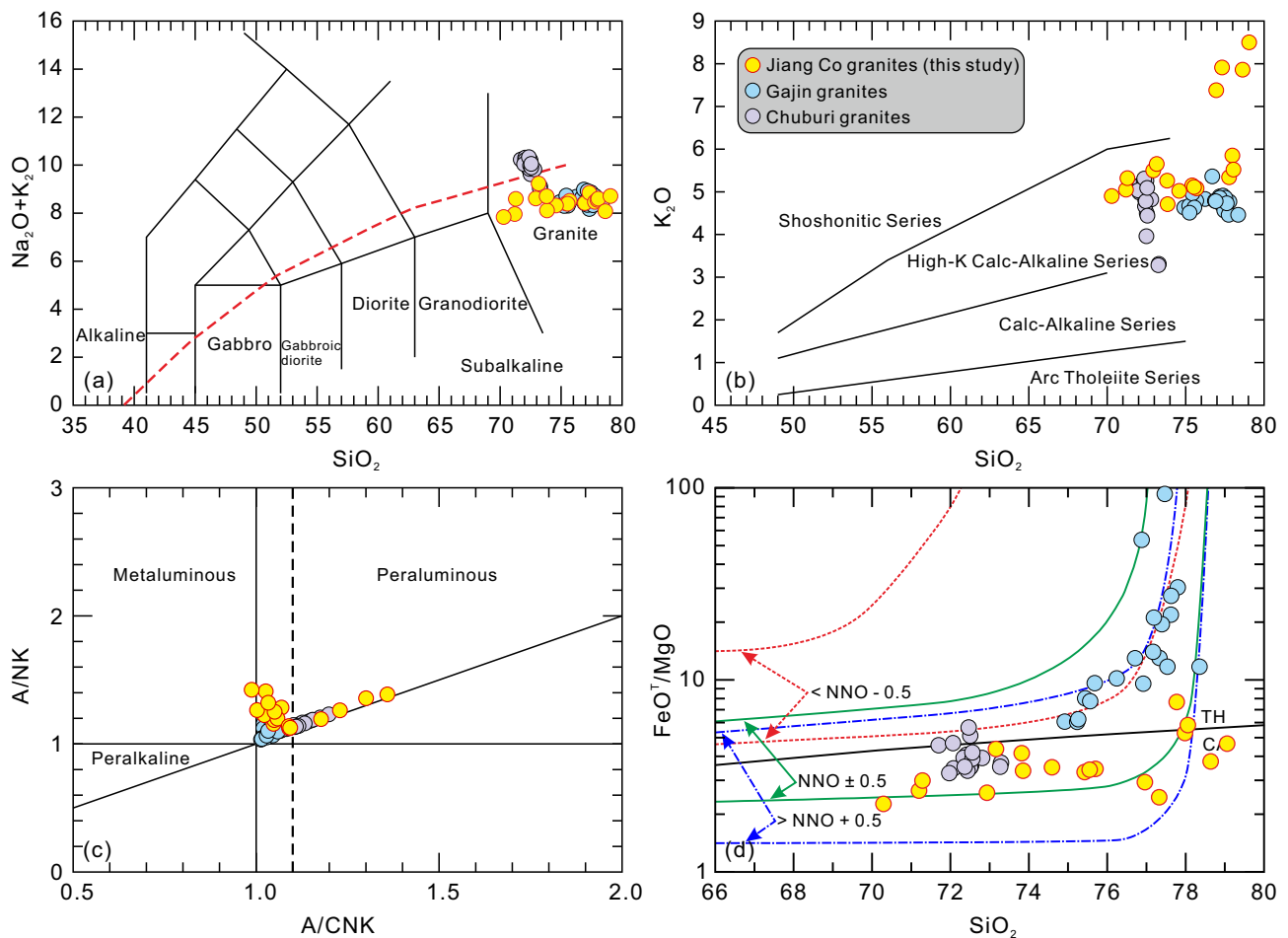

Fig. 4. (a) Total alkalis versus silica diagram (Middlemost 1994); (b) K_2O versus SiO_2 diagram (Peccerillo and Taylor 1976); (c) A/NK versus A/CNK diagram (Maniar and Piccoli 1989); (d) FeO^T/MgO versus SiO_2 diagram (Sisson et al. 2005); the sloped line separates tholeiitic (TH) from calc-alkaline (CA) magmas using the criterion of Miyashiro (1974). Data for the Gajin granites in the Lhasa terrane are from Yang et al. (2019), and for the Chuburi granites in the southern Qiangtang subterrane are from He et al. (2019).
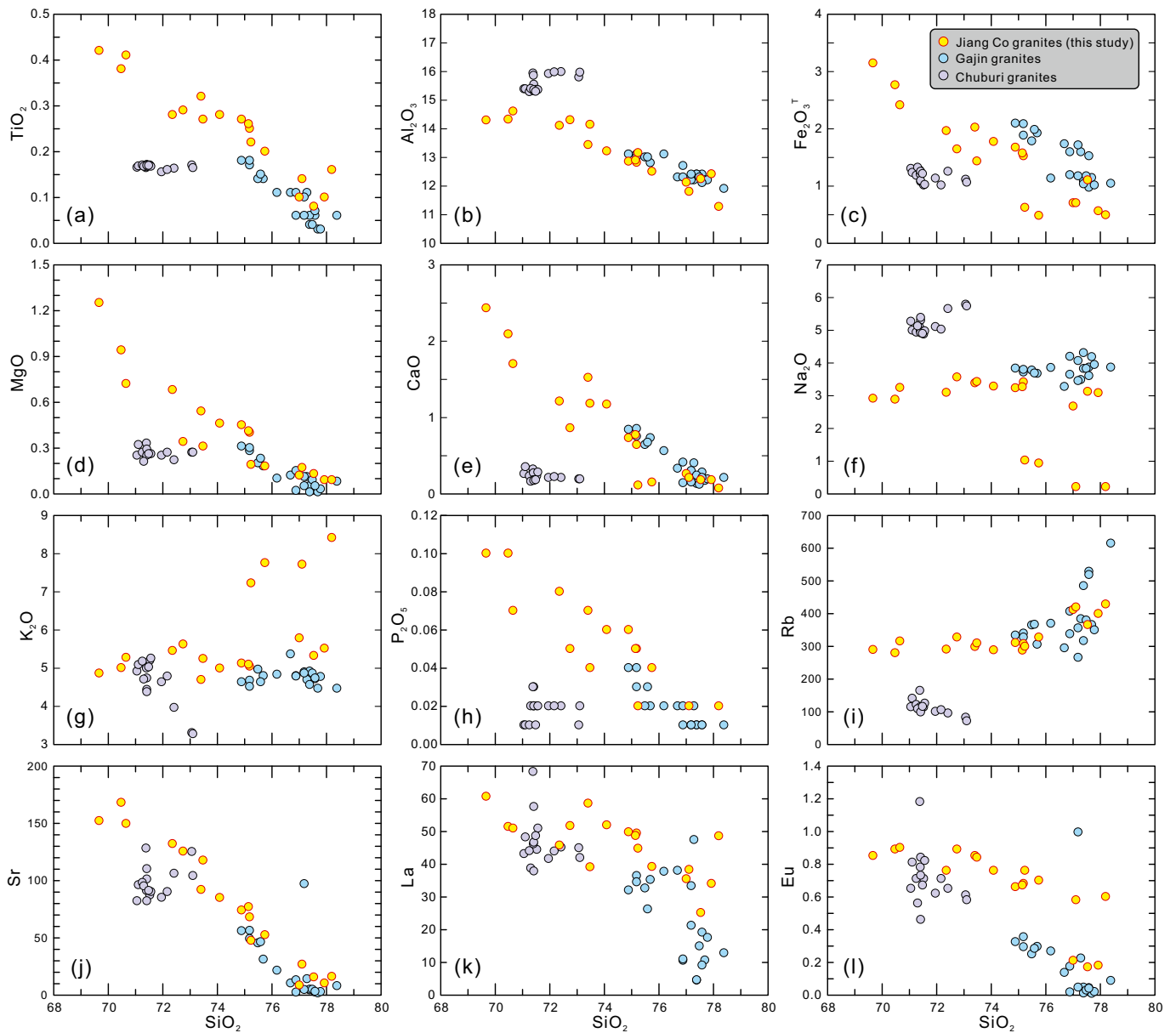
Fig. 5. Selected whole-rock major and trace element variation diagrams.
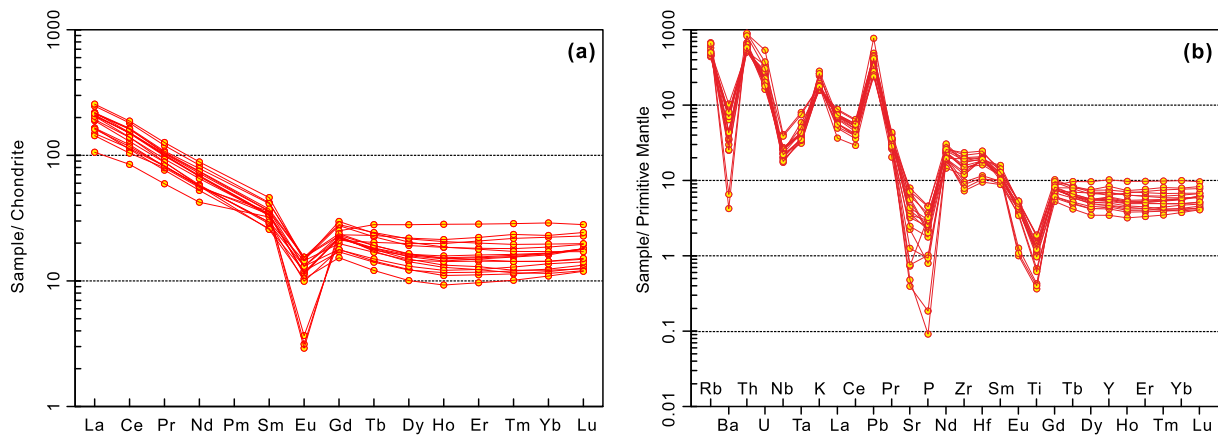

Fig. 6. (a) Chondrite–normalized REE patterns and (b) primitive mantle–normalized trace element spider diagram for the Jiang Co granites. Chondrite and primitive mantle normalization values are from Sun and Mcdonough (1989).
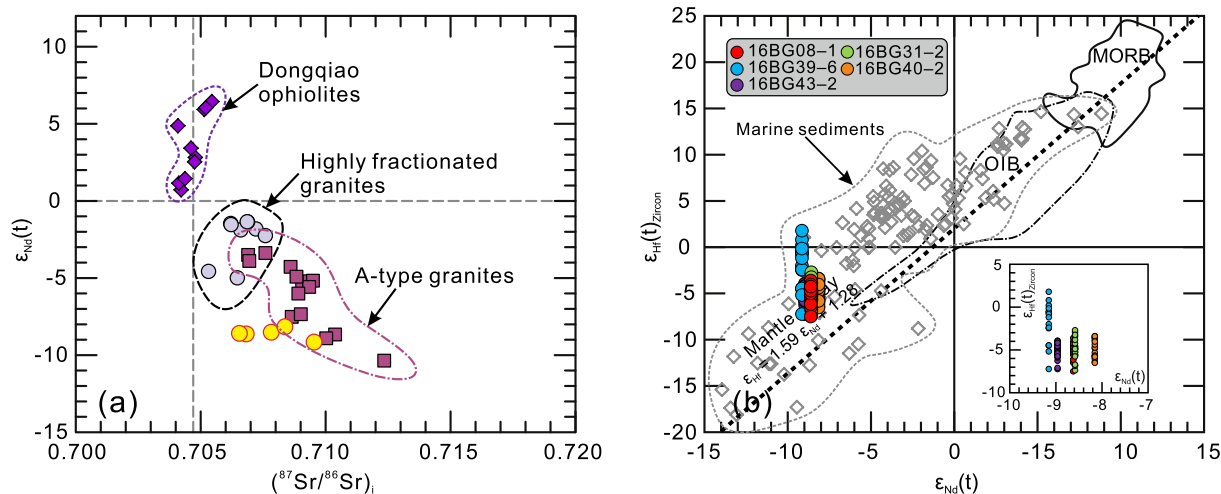
Fig. 7. (a) Whole-rock $\varepsilon_{Nd}(t)$ versus $({}^{87}Sr/{}^{86}Sr)_i$ diagram and (b) zircon $\varepsilon_{Hf}(t)$ versus whole-rock $\varepsilon_{Nd}(t)$ diagram for the Jiang Co granites. Data for the Dongqiao ophiolites are from Liu et al. (2016), for the Baingoin A-type granites are from Qu et al. (2012), for the highly fractionated I-type granites are from He et al. (2019), and for the marine sediments are from Vervoort et al. (1999, 2011).

values of 0.282498–0.282590 and $\varepsilon_{Hf}(t)$ values of -7.2 to -3.9, with the corresponding T_{Hf}^{2DM} ages varying from 1.63–1.42 Ga (Fig. 8e).

5. Discussion

5.1. Petrogenesis

5.1.1. Fractional crystallization

The Jiang Co granites have high SiO_2 (up to 78 wt%) and total alkali ($K_2O + Na_2O = 7.8$–9.2 wt%) contents, and low $Fe_2O_3^T$, TiO_2, MgO, Sr, Ba, and Eu concentrations, indicating that these rocks have experienced fractional crystallization (Wu et al., 2003). The A/CNK ratios for most Jiang Co granites are below 1.1, however, four samples (16BG31–1, 16BG31–2, 16BG43–1 and 16BG43–2) display high A/CNK ratios (>1.1), suggesting that the four samples were formed by extensive fractionation of feldspar that lead to a significant decrease in CaO and Na_2O (Fig. 5e, f; Wang et al., 2015). On Harker diagrams, these granites show broadly linear trends (Fig. 5). The Al_2O_3 and CaO contents decrease with increasing SiO_2 contents for these granites (Fig. 5b, e), indicating that plagioclase and/or K-feldspar fractionated from the magma. This process is confirmed by the slight negative slope between the Na_2O and SiO_2 and the positive correlation between K_2O and SiO_2 for the Jiang Co granites (Fig. 5f, g). Quantitative modeling also indicate that the highly evolved sample 16BG43–1 may be generated by 70–80% fractionation of 60% plagioclase, 25% K-feldspar, and 15% biotite from less evolved magma (16BG39–6). The negative correlations between SiO_2 and TiO_2, $Fe_2O_3^T$, MgO, and P_2O_5 (Fig. 5a, c, d, and h) suggest the fractionation of biotite, apatite, and Fe–Ti oxides from the magmas.

Additionally, trace element variations also indicate that fractional crystallization occurred (Fig. 9). Generally, the fractionation of plagioclase can result in negative Sr and Eu anomalies, and induce high Rb contents and Rb/Sr ratios, whereas the fractionation of K-feldspar leads to negative Ba and Eu anomalies (Wu et al. 2003). The Jiang Co granites generally plot between plagioclase and K-feldspar fractionation trend lines, indicating that plagioclase and K-feldspar were the dominant minerals fractionated during magmatic evolution (Fig. 9a–c). This is also confirmed by significant depletions in Sr, Ba, and Eu on the primitive mantle-normalized trace element diagrams (Fig. 6b). The decrease in REE contents with increasing SiO_2 contents suggests the separation of accessory minerals, including apatite, titanite, zircon, allanite, and monazite. The diagram of $(La/Yb)_N$ versus La (Fig. 9d) shows that the fractionation of the accessory minerals in granitic melt, and the variation

in REE contents is consistent with the fractionation of monazite and allanite, whereas the influence of apatite, titanite, and zircon is unclear. Negative Nb, Ta, Ti, and P anomalies on the primitive mantle-normalized trace element diagrams are commonly attributed to the fractionation of ilmenite, titanite, and apatite (Fig. 6b). Quantitative modeling reveals that the REE abundances of highly evolved samples can be generated by 0.5–1.5% fractional crystallization of 90% apatite, 5% allanite, and 5% titanite from the assumed starting compositions (16BG39–6) (Fig. 10).

In summary, fractional crystallization played an important role in the formation of the late Early Cretaceous Jiang Co granites. Fractionation of K-feldspar and plagioclase is the main cause of the variation in major elements and Rb, Sr Eu, and Ba contents. The variation of trace-element compositions was controlled mainly by the fractionation of ilmenite, apatite, titanite, and allanite.

5.1.2. Sources characteristics and partial melting conditions

The Jiang Co Cretaceous granites consist of quartz, K-feldspar, and plagioclase with minor biotite, and no hornblende and alkalic mafic minerals have been identified. Using the calibration of Boehnke et al. (2013), whole-rock Zr saturation temperatures (T_{Zr}) of the Jiang Co granites range from 696 to 757 °C with a mean of 722 °C, which are lower than those of typical A-type granites. In addition, the Zr + Nb + Ce + Y contents (< 350 ppm), $10,000 \times$ Ga/Al (1.48–2.26) and FeO^T/MgO (< 11) values of these granites are also lower than those of A-type granite (Whalen et al., 1987). The Jiang Co granites have high Rb/Sr (1.7–49.1) ratios and rather low Nb/Ta (7.1–12.6) and Zr/Hf (21.8–35.1) ratios, indicating that these rocks are the highly evolved granites (e.g., Guo et al. 2012; Wu et al., 2017; Zeng and Gao 2017). Additionally, the Jiang Co granites are geochemically similar to the high-silica granites described by Lee and Morton (2015) and Wu et al., (2017), including high SiO_2 (69.7–78.2 wt%) and K_2O (4.7–8.4 wt%) contents (Fig. 5). Therefore, the Jiang Co granites are of high-silica granites, similar to the adjacent Gajin granites in the Lhasa terrane (Yang et al., 2019) and the Chuburi granites in the southern Qiangtang subterrane (He et al., 2019).

High-silica granites can be produced by (1) advanced fractional crystallization (Ji et al. 2020; Putirka et al., 2014; Sisson et al., 2005), and (2) low-degree partial melting of preexisting infracrustal rocks (Frost et al., 2016; Glazner et al., 2008). The Jiang Co granites have high initial ${}^{87}Sr/{}^{86}Sr$ (0.7066 to 0.7095) ratios and negative $\varepsilon_{Nd}(t)$ (-8.2 to -9.2) values (Fig. 7a), with T_{Nd}^{2DM} ages of 1.66–1.58 Ga. These data suggest
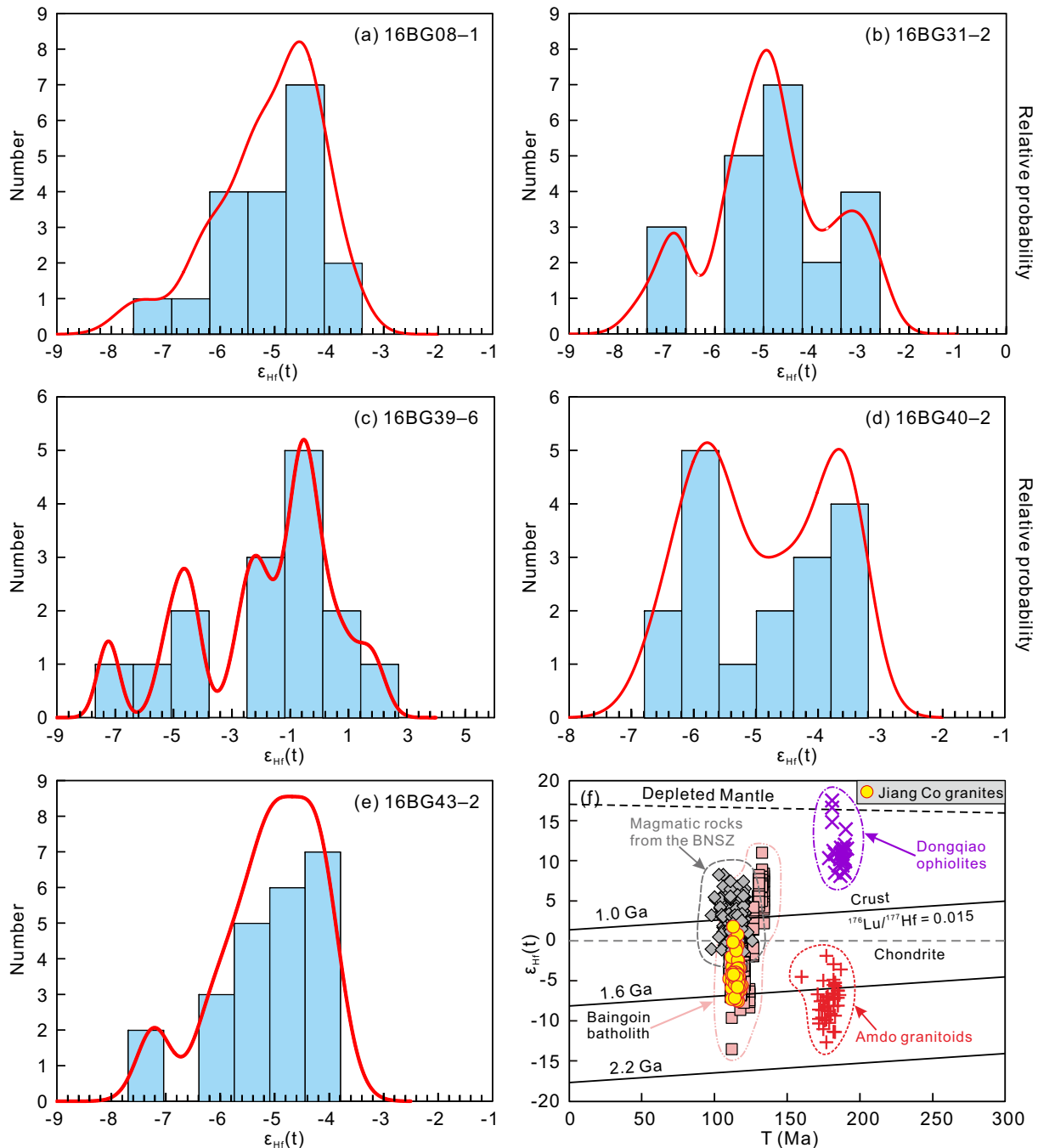
Fig. 8. (a–e) Histograms of zircons $\varepsilon_{Hf}(t)$ values for the Jiang Co granites. (f) Plot of zircon $\varepsilon_{Hf}(t)$ values versus U–Pb ages. Data for the Dongqiao ophiolites are from Liu et al. (2016), for the magmatic rocks in the BNSZ are from Hu et al. (2017), and for the Amdo granitoids are from Liu et al. (2017).

that the Jiang Co granites were derived mostly from the Mesoproterozoic continental crust. Zircon in the Jiang Co granites has negative to positive $\varepsilon_{Hf}(t)$ values ranging from −7.5 to 1.8 (Fig. 7b), and yields two-stage Hf model ages (T_{Hf}^{2DM}) of 1.65–1.05 Ga. These Hf isotopic characteristics are similar to those of late Early Cretaceous granitoids and volcanic rocks in the Baingoin−Dongqiao areas (Fig. 8f; Hu et al., 2017; Zhu et al., 2016), suggesting that the source rocks of granites may be mainly related to the recycling of ancient crustal materials in the central Tibet. The inherited zircon grains with variable ages (1042–158 Ma) in the Jiang Co granites may be derived from either crustal wall rocks during magma ascending or directly inherited from their sources. Available experimental studies reveal that monzogranitic melts were

derived from melting of mafic rocks at low temperature (Gao et al., 2016; Sisson et al., 2005; Topuz et al., 2010), whereas granodioritic-tonalitic melts were produced by dehydration melting of mafic rocks at high temperature (Gao et al., 2016; Rapp and Watson, 1995; Springer and Seck, 1997). The Jiang Co granites display high and variable SiO_2 (69.7–78.2 wt%) and K_2O (4.7–8.4 wt%) contents, and K_2O/Na_2O (1.39–39.67) ratios, and resemble monzogranitic melts from K-rich basaltic compositions (Annen et al., 2005; Gao et al., 2016). The Jiang Co granites show low FeO^T/MgO ratios and fall mainly in the calc-alkaline field, corresponding to intermediate-to-high fO_2 field (Fig. 4d), indicating the involvement of high-fO_2 materials (Sisson et al., 2005). The high Th/La (0.72–2.99) ratios of the Jiang Co granites suggest melting of the
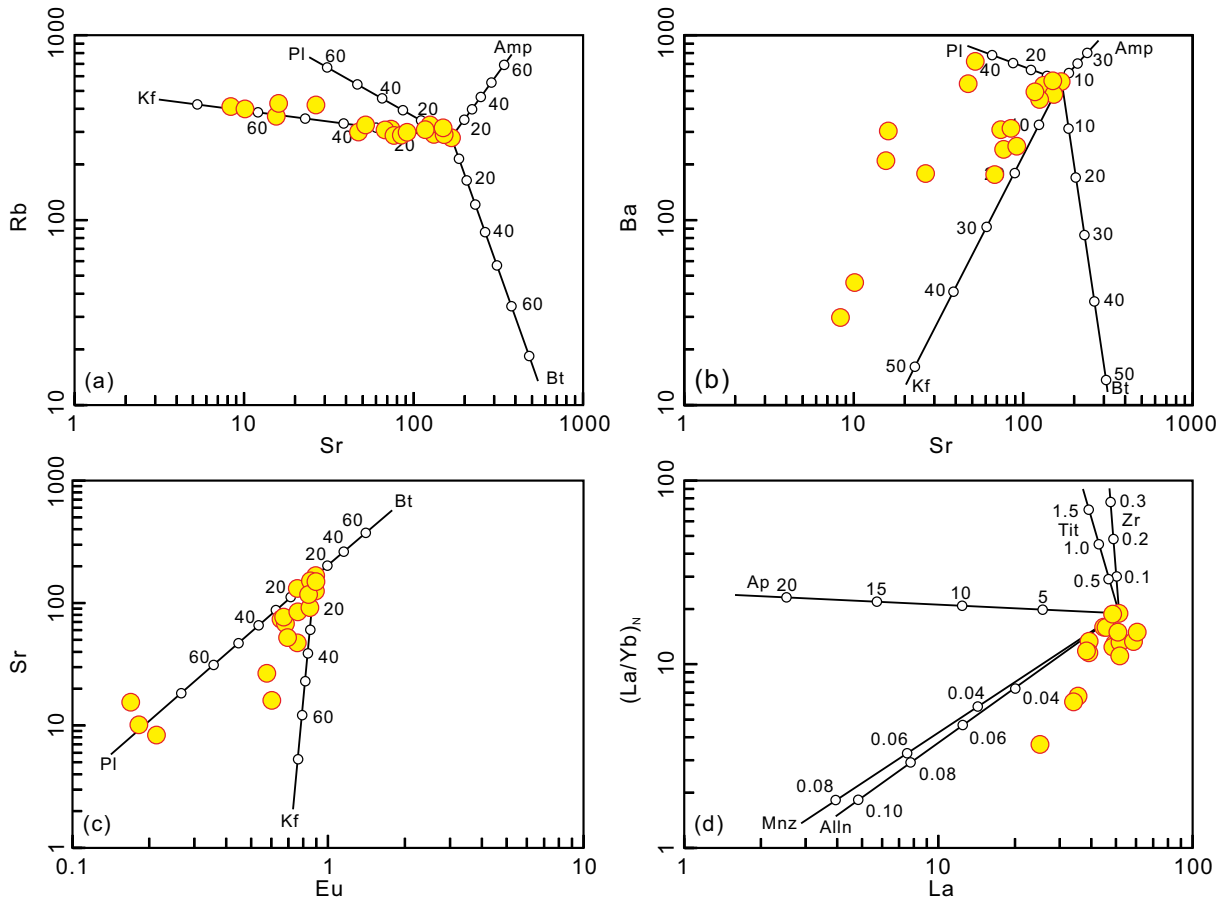
Fig. 9. (a) Rb versus Sr, (b) Ba versus Sr, and (c) Sr versus Eu diagrams, showing that the fractionation of feldspar plays an important role in the formation of the Jiang Co granites. Partition coefficients for Ba and Sr are from Hanson (1978), and for Eu is from Arth (1976). (d) $(La/Yb)_N$ versus La diagram, showing the change of REE patterns due to the fractionation of accessory minerals. Partition coefficients are from Fujimaki (1986) for apatite, Green and Pearson (1986) for titanite, Mahood and Hildreth (1983) for zircon and allanite, and Yurimoto et al. (1990) for monazite. Mineral abbreviations: Alln = allanite, Amp = amphibole, Ap = apatite, Bt = biotite, Kf = K-feldspar, Mnz = monazite, Pl = plagioclase, Tit = titanite, Zr = zircon.

source region involving sediments. Therefore, Jiang Co granites were generated by fluid-present partial melting of infracrustal ancient materials, and subsequently experienced extensive fractional crystallization during magma evolution, and eventually emplaced at shallow crustal levels.

Fig. 10. REE modeling results. The assumed parent magma composition is represented by the least fractionated sample 16BG39–6. Partition coefficients are from Arth (1976) and Hanson (1978).

5.2. Geodynamic processes

The formation of high-silica granites is related to accretionary and collisional orogenic processes (Jung et al., 2012; Wu et al., 2020). These granites can be generated in a continental arc setting or a post-collisional extensional regime after crustal thickening (Bagdonas et al., 2016; Clemens et al., 2009; Duggen et al., 2005; Roberts and Clemens, 1993; Topuz et al., 2010). In an Andean-type continental arc setting, these granites are derived from the partial melting of thickened crust and lithosphere, and undergo a longer differentiation process (Lee et al., 2007; Lee and Morton, 2015). Such granites are generally associated with gabbro–diorite–tonalite–granodiorite associations (Lee et al., 2007; Pitcher, 1997). However, in post-collisional settings similar to that of the Himalayan leucogranites, the formation of high-silica granites may be related to continental collision and subsequent crustal thickening and slab breakoff or lithospheric delamination (Bird, 1979; Davies and von Blanckenburg, 1995; Ji et al., 2020; Le Fort, 1981). These processes induce the partial melting of the asthenosphere and the overriding metasomatized lithosphere, leading to mafic magmatism, and subsequently generate crust-derived magmatism by crustal anatexis resulting from conductive heating due to the upwelling of the asthenosphere and mantle-derived magma underplating the crust (Zhu et al., 2015).

Voluminous Mesozoic magmatic rocks are widely distributed along the Lhasa–Qiangtang collisional belt (Zhu et al., 2016 and references therein) because of the subduction of oceanic lithosphere and subsequent collision or post-collisional processes. The Baingoin–Dongqiao
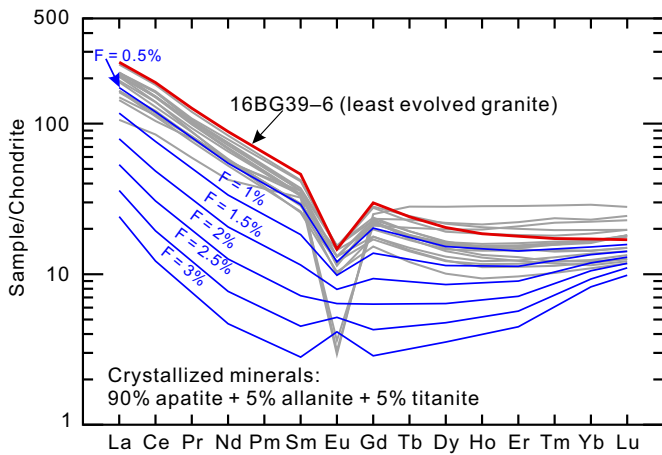
areas are located in the middle-eastern segment of the BNSZ, and contain abundant magmatic activities, including Jurassic andesitic rocks (Hu et al., 2020;Tang et al., 2019; Zeng et al., 2016) and Cretaceous intermediate-felsic rocks (He et al., 2019; Hu et al. 2017, 2019; Liu et al., 2017; Qu et al., 2012; Yang et al., 2019). The Middle-Late Jurassic andesitic rocks (165–161 Ma) were mainly identified in the Daru Tso and Jiaqiong areas, and derived from interaction between partial melting of subducted sediments and overlying mantle peridotite. These andesitic rocks formed in an arc setting related to the subduction of the Bangong–Nujiang Tethys oceanic lithosphere (Tang et al., 2019; Zeng et al., 2016). The Cretaceous magmatic rocks (126–102 Ma) were more widely distributed than the Jurassic magmatic rocks in both sides of and within the middle-eastern segments of the BNSZ (Fig. 1b). These rocks consist of andesites, rhyolites, granodiorites and granites, and are related to the post-collisional extensional setting following the collision of the northern Lhasa and southern Qiangtang subterranes (Hu et al. 2017, 2019; Kapp and Decelles, 2019; Liu et al., 2017; Zhu et al., 2016). Meanwhile, the A_2-type granites (ca. 110 Ma) identified in the northern Lhasa subterrane also indicate a post-collisional setting (Qu et al., 2012). Additionally, sedimentary provenance and age-spectra of detrital zircons of the Early Cretaceous strata (Duba and Duoni Formations) from our study area indicate that the Lhasa–Qiangtang collision took place during the late Early Cretaceous (122–113 Ma) (Lai et al., 2019; Zhu et al., 2019). To the west of the study area in the Nyima basin, major deformation and denudation occurred at ca. 125–118 Ma, resulting in an evolution from marine to non-marine environments. This indicates that the Lhasa–Qiangtang collision was well underway in the late Early Cretaceous (Kapp et al., 2007; Kapp and Decelles, 2019). The latest paleomagnetic results of the Middle Jurassic limestones from the Shuanghu area in the southern Qiangtang subterrane indicate that the width of the BNTO was 2,600 ± 710 km (23.4° ± 6.4°) in the Middle Jurassic time (Cao et al., 2019). The Jiang Co granites were also formed during the late Early Cretaceous (ca.114 Ma), and have similar $\varepsilon_{Hf}(t)$ values to the Cretaceous intermediate-felsic rocks in the Baingoin–Dongqiao areas (Fig. 8f). Therefore, combined with regional geological data, in particular adjacent Middle-Late Jurassic arc magmatic rocks (Liu et al., 2017; Zeng et al., 2016), Cretaceous sedimentary rocks (Lai et al. 2019; Zhu et al., 2019), and contemporaneous magmatic activity (Hu et al. 2017, 2019; Zhu et al., 2016 and references therein), we suggest that these rocks were generated in a post-collisional setting.

Both slab breakoff and lithospheric delamination after collision have been proposed to account for the tectonic setting of high-K calc-alkaline granitoids in a post-collisional setting (Coulon et al., 2002; Davies and von Blanckenburg, 1995; Whalen et al., 2006). Zircon U–Pb ages and Hf isotopic compositions of the Cretaceous magmatic rocks along the BNSZ reveal the presence of a magmatic flare-up with compositional diversity at ~114 Ma (Fig. 8f; Hu et al. 2019), which is attributed to the slab breakoff rather than lithospheric delamination. This interpretation is further corroborated by the Late Cretaceous adakitic rocks (~94 Ma) (Yi et al., 2018) and the A_2-type granites (ca. 113–109 Ma) (Chen et al., 2014; Qu et al., 2012) from the Baingon-Xainza areas in the northern Lhasa subterrane. The cessation of arc magmatism and a substantial amount of topographic uplift took place the northern margin of the Nyima basin after the initial collision between the Lhasa and Qiangtang terranes (Kapp et al,. 2007; Kapp and Decelles, 2019; Zhu et al. 2016 and references therein). These phenomena can be regarded as the indicator of the occurrence of slab breakoff, similar to many elevated areas on Earth, such as the Apennines and Western Alps (Nocquet et al., 2016; van der Meulen et al., 1999). The initial Lhasa–Qiangtang collision likely occurred at 125–118 Ma, which revealed by the stratigraphic and sedimentary characteristics in the adjacent areas (Nyima and Baingoin basin) (Kapp et al., 2007; Lai et al., 2019; Zhu et al., 2019). Numerical modeling results indicate that slab breakoff possibly took place at ~15–10 Ma after the initial continent collision (Freeburn et al.,
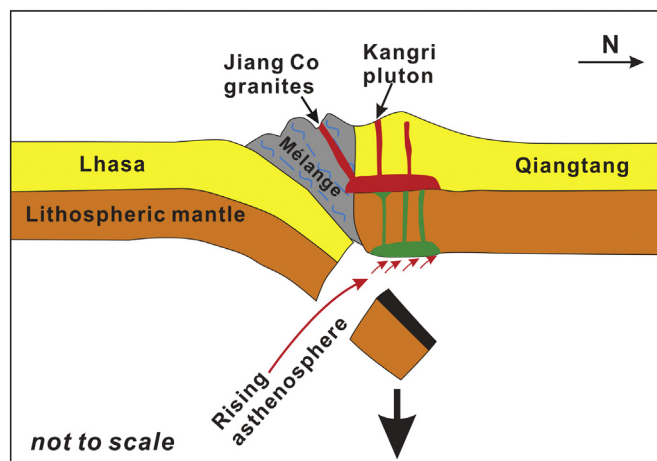

Fig. 11. Simplified geodynamic model for the Cretaceous evolution of the middle-eastern segments of the Bangong–Nujiang suture zone, central Tibet. The model is developed based on ideas and/or data in the following references: Hu et al. (2017, 2019, 2020); Kapp et al. (2005, 2007); Kapp and Decelles (2019); Liu et al. (2016, 2017); Qu et al. (2012); Wang et al. (2016); Yang et al. (2019); Zeng et al. (2016); Zhong et al. (2017); Zhu et al. (2016).

2017; van Hunen and Allen, 2011). This model fits a scenario with initial Lhasa–Qiangtang collision at ~125–118 Ma and slab breakoff at ~114 Ma. The Jiang Co granites in the BNSZ were formed in a post-collisional extensional setting during the late Early Cretaceous time (115–113 Ma). In combination with rapid topographic uplift (Kapp et al., 2007), A_2-type granites (Qu et al., 2012), and coeval intermediate-felsic rocks (Hu et al. 2017, 2019; Zhu et al., 2016), we suggest that the formation of late Early Cretaceous magmatism was related to slab breakoff after the Lhasa–Qingtang collision (Fig. 11). Under a slab breakoff setting, the upwelling of asthenosphere mantle through the slab window leads to thermal anomaly of the overlying lithosphere. These processes trigger partial melting of the asthenosphere and the overriding metasomatized lithosphere, producing basaltic magmatism that leads to granitic magmatism in the crust (Davies and von Blanckenburg, 1995). In this case, the Jiang Co granites (~114 Ma) can be interpreted as the consequence of the slab breakoff of the Bangong–Nujiang Tethys oceanic lithosphere. These rocks were derived by partial melting of ancient crustal materials, and subsequently experienced extensive fractional crystallization.

6. Conclusions

(1) The Jiang Co pluton is located within the BNSZ. Zircon U–Pb ages suggest that these rocks were formed at ca.114 Ma.

(2) The Jiang Co granites have high SiO_2 and K_2O contents, and K_2O/Na_2O ratios, corresponding to high-silica granites. Petrological and geochemical characteristics imply that these granites were formed by partial melting of ancient crustal materials, and subsequently experienced extensive differentiation, and eventually emplaced at shallow crustal levels.

(3) Along with adjacent magmatic activity and sedimentary rocks, we suggest that the Jiang Co granites were generated in a post-collisional setting, resulting from slab breakoff after collision between the Qiangtang and Lhasa terranes.

Declaration of Competing Interest

The authors declare that they have no known competing financial interests or personal relationships that could have appeared to influence the work reported in this paper.

Acknowledgments

Appendix A. Supplementary data

Supplementary data to this article can be found online at https://doi.org/10.1016/j.lithos.2020.105788.

References

Andersen, T., 2002. Correction of common lead in U–Pb analyses that do not report [204]Pb. Chem. Geol. 192, 59–79.

Annen, C., Blundy, J., Sparks, R., 2005. The genesis of intermediate and silicic magmas in deep crustal hot zones. J. Petrol. 47, 505–539.

Arth, J.G., 1976. Behaviour of trace elements during magmatic processes: a summary of theoretical models and their applications. J. Res. U.S. Geol. Surv. 4, 41–47.

Bachmann, O., Bergantz, G.W., 2008. Rhyolites and their source mushes across tectonic settings. J. Petrol. 49, 2277–2285.

Bagdonas, D.A., Frost, C.D., Fanning, C.M., 2016. The origin of extensive Neoarchean high-silica batholiths and the nature of intrusive complements to silicic ignimbrites: Insights from the Wyoming batholith, U.S.A. Am. Mineral. 101, 1332–1347.

Bird, P., 1979. Continental delamination and the Colorado Plateau. J. Geophys. Res. 84, 7561–7571.

Boehnke, P., Watson, E.B., Trail, D., Harrison, T.M., Schmitt, A.K., 2013. Zircon saturation re-revisited. Chem. Geol. 351, 324–334.

Cao, Y., Sun, Z., Li, H., Pei, J., Liu, D., Zhang, L., Ye, X., Zheng, Y., He, X., Ge, C., Jiang, W., 2019. New Paleomagnetic Results From Middle Jurassic Limestones of the Qiangtang terrane, Tibet: Constraints on the Evolution of the Bangong–Nujiang Ocean. Tectonics 38, 215–232.

Chen, Y., Zhu, D.C., Zhao, Z.D., Meng, F.Y., Wang, Q., Santosh, M., Wang, L.Q., Dong, G.C., Mo, X.X., 2014. Slab breakoff triggered ca. 113 Ma magmatism around Xainza area of the Lhasa Terrane, Tibet. Gondw. Res. 26, 449–463.

Clemens, J.D., Darbyshire, D.P.F., Flinders, J., 2009. Sources of post-orogenic calcalkaline magmas: The Arrochar and Garabal Hill-Glen Fyne complexes, Scotland. Lithos 112, 524–542.

Coulon, C., Fourcade, S., Maury, R., Bellon, H., Louni-Hacini, A., Cotten, J., Coutelle, A., Hermitte, D., 2002. Post-collisional transition from calc-alkaline to alkaline volcanism during the Neogene in Oranie (Algeria): magmatic expression of a slab breakoff. Lithos 62, 87–110.

Dan, W., Wang, Q., Zhang, X.Z., Tang, G.J., 2020. Early Paleozoic S-type granites as the basement of Southern Qiantang Terrane, Tibet. Lithos 356–357, 105395.

Davies, J.H., von Blanckenburg, F., 1995. Slab breakoff: A model of lithosphere detachment and its test in the magmatism and deformation of collisional orogens. Earth Planet. Sci. Lett. 129, 85–102.

Duggen, S., Hoernle, K., Van Den Bogaard, P., Garbe-SchÖNberg, D., 2005. Post-collisional transition from subduction- to intraplate-type magmatism in the Westernmost Mediterranean: Evidence for continental-edge delamination of subcontinental lithosphere. J. Petrol. 46, 1155–1201.

Fan, J.J., Li, C., Xie, C.M., Wang, M., Chen, J.W., 2015. Petrology and U–Pb zircon geochronology of bimodal volcanic rocks from the Maierze Group, northern Tibet: constraints on the timing of closure of the Banggong–Nujiang Ocean. Lithos 227, 148–160.

Freeburn, R., Bouilhol, P., Maunder, B., Magni, V., Van Hunen, J., 2017. Numerical models of the magmatic processes induced by slab breakoff. Earth Planet. Sci. Lett. 478, 203–213.

Frost, C.D., Swapp, S.M., Frost, B.R., Finley-Blasi, L., Fitz-Gerald, D.B., 2016. Leucogranites of the Teton Range, Wyoming: A record of Archean collisional orogeny. Geochim. Cosmochim. Acta 185, 528–549.

Fujimaki, H., 1986. Partition coefficients of Hf, Zr, and REE between zircon, apatite, and liquid. Contrib. Mineral. Petrol. 94, 42–45.

Gao, P., Zheng, Y., Zhao, Z.F., 2016. Experimental melts from crustal rocks: A lithochemical constraint on granite petrogenesis. Lithos 133–157.

Gao, L.E., Zeng, L., Asimow, P.D., 2017. Contrasting geochemical signatures of fluid–absent versus fluid–fluxed melting of muscovite in metasedimentary sources: the Himalayan leucogranites. Geology 45, 39–42.

Glazner, A.F., 2014. Magmatic life at low Reynolds number. Geology 42, 935–938.

Glazner, A.F., Coleman, D.S., Bartley, J.M., 2008. The tenuous connection between high-silica rhyolites and granodiorite plutons. Geology 36, 183–186.

Green, T.H., Pearson, N.J., 1986. Rare-earth element partitioning between sphene and coexisting silicate liquid at high pressure and temperature. Chem. Geol. 55, 105–119.

Guo, C., Chen, Y., Zeng, Z., Lou, F., 2012. Petrogenesis of the Xihuashan granites in southeastern China: constraints from geochemistry and in-situ analyses of zircon U–Pb Hf–O isotopes. Lithos 148, 209–227.

Guynn, J.H., Kapp, P., Pullen, A., Heizler, M., Gehrels, G., Ding, L., 2006. Tibetan basement rocks near Amdo reveal "missing" Mesozoic tectonism along the Bangong suture, central Tibet. Geology 34, 505–508.

Guynn, J., Kapp, P., Gehrels, G., Ding, L., 2012. U–Pb geochronology of basement rocks in central Tibet and paleogeographic implications. J. Asian Earth Sci. 43, 23–50.

Hanson, G.N., 1978. The application of trace elements to the petrogenesis of igneous rocks of granitic composition. Earth Planet. Sci. Lett. 38, 26–43.

Hao, L.L., Wang, Q., Wyman, D.A., Ou, Q., Dan, W., Jiang, Z.Q., Wu, F.Y., Yang, J.H., Long, X.P., Li, J., 2016. Underplating of basaltic magmas and crustal growth in a continental arc: Evidence from Late Mesozoic intermediate–felsic intrusive rocks in southern Qiangtang, central Tibet. Lithos 245, 223–242.

Hao, L.L., Wang, Q., Zhang, C.F., Ou, Q., Yang, J.H., Dan, W., Jiang, Z.Q., 2019. Oceanic plateau subduction during closure of the Bangong-Nujiang Tethyan Ocean: Insights from central Tibetan volcanic rocks. Geol. Soc. Am. Bull. 131, 864–880.

He, H.Y., Li, Y.L., Wang, C.S., Han, Z.P., Ma, P.F., Xiao, S., 2019. Petrogenesis and tectonic implications of Late Cretaceous highly fractionated I-type granites from the Qiangtang block, central Tibet. J. Asian Earth Sci. 176, 337–352.

Hoskin, P.W.O., Schaltegger, U., 2003. The Compositions of Zircon and Igneous and Metamorphic Petrogenesis. Rev. Mineral. Geochem. 53, 27–55.

Hu, P.Y., Zhai, Q.G., Jahn, B.M., Wang, J., Li, C., Chung, S.L., Lee, H.Y., Tang, S., 2017. Late Early Cretaceous magmatic rocks (118–113Ma) in the middle segment of the Bangong–Nujiang suture zone, Tibetan Plateau: Evidence of lithospheric delamination. Gondw. Res. 44, 116–138.

Hu, W.L., Wang, Q., Yang, J.H., Zhang, C., Tang, G.J., Ma, L., Qi, Y., Yang, Z.Y., Sun, P., 2019. Late early Cretaceous peraluminous biotite granites along the Bangong–Nujiang suture zone, Central Tibet: Products derived by partial melting of metasedimentary rocks? Lithos 344–345, 147–158.

Hu, W.L., Wang, Q., Yang, J.H., Tang, G.J., Qi, Y., Ma, L., Yang, Z.Y., Sun, P., 2020. Amphibole and whole-rock geochemistry of early Late Jurassic diorites, Central Tibet: Implications for petrogenesis and geodynamic processes. Lithos 370–371, 105644.

van Hunen, J., Allen, M.B., 2011. Continental collision and slab break-off: a comparison of 3-D numerical models with observations. Earth Planet. Sci. Lett. 302, 27–37.

Jackson, S.E., Pearson, N.J., Griffin, W.L., Belousova, E.A., 2004. The application of laser ablation-inductively coupled plasma-mass spectrometry to in situ U–Pb zircon geochronology. Chem. Geol. 211, 0–69.

Ji, W.Q., Wu, F.Y., Liu, X.C., Liu, Z.C., Zhang, C., Liu, T., Wang, J.G., Paterson, S.R., 2020. Pervasive Miocene melting of thickened crust from the Lhasa terrane to Himalaya, southern Tibet and its constraint on generation of Himalayan leucogranite. Geochim. Cosmochim. Acta 278, 137–156.

Jung, S., Mezger, K., Nebel, O., Kooijman, E., Berndt, J., Hauff, F., Münker, C., 2012. Origin of Meso-Proterozoic post-collisional leucogranite suites (Kaokoveld, Namibia): constraints from geochronology and Nd, Sr, Hf, and Pb isotopes. Contrib. Mineral. Petrol. 163, 1–17.

Kapp, P.A., Decelles, P.G., 2019. Mesozoic–Cenozoic geological evolution of the Himalayan-Tibetan orogen and working tectonic hypotheses. Am. J. Sci. 319, 159–254.

Kapp, P., Yin, A., Harrison, T.M., Ding, L., 2005. Cretaceous-Tertiary shortening, basin development, and volcanism in central Tibet. Geol. Soc. Am. Bull. 117, 865–878.

Kapp, P., DeCelles, P.G., Gehrels, G.E., Heizler, M., Ding, L., 2007. Geological records of the Lhasa–Qiangtang and Indo-Asian collisions in the Nima area of central Tibet. Geol. Soc. Am. Bull. 119, 917–932.

Lai, W., Hu, X., Garzanti, E., Xu, Y., Ma, A., Li, W., 2019. Early Cretaceous sedimentary evolution of the northern Lhasa terrane and the timing of initial Lhasa-Qiangtang collision. Gondw. Res. 73, 136–152.

Le Fort, P., 1981. Manaslu leucogranite: a collision signature of the Himalaya: a model for its genesis and emplacement. J. Geophys. Res. Solid Earth 86, 10545–10568.

Lee, C.T.A., Morton, D.M., 2015. High silica granites: Terminal porosity and crystal settling in shallow magma chambers. Earth Planet. Sci. Lett. 409, 23–31.

Lee, C.T.A., Morton, D.M., Kistler, R.W., Baird, A.K., 2007. Petrology and tectonics of Phanerozoic continent formation: From island arcs to accretion and continental arc magmatism. Earth Planet. Sci. Lett. 263, 370–387.

Lee, C.T.A., Morton, D.M., Farner, M.J., Moitra, P., 2015. Field and model constraints on silicic melt segregation by compaction/hindered settling: the role of water and its effect on latent heat release. Am. Mineral. 100, 1762–1777.

Li, X.H., Sun, M., Wei, G.J., Liu, Y., Lee, C.Y., Malpas, J., 2000. Geochemical and Sm–Nd isotopic study of amphibolites in the Cathaysia Block, southeastern China: evidence for an extremely depleted mantle in the Paleoproterozoic. Precambrian Res. 102, 251–262.

Li, X.H., Zhou, H., Chung, S.L., Lo, C.H., Wei, G., Liu, Y., Lee, C.Y., 2002. Geochemical and Sr–Nd isotopic characteristics of late Paleogene ultrapotassic magmatism in southeastern Tibet. Int. Geol. Rev. 44, 559–574.

Li, X.H., Liu, D.Y., Sun, M., Li, W.X., Liang, X.R., Liu, Y., 2004. Precise Sm–Nd and U–Pb isotopic dating of the supergiant Shizhuyuan polymetallic deposit and its host granite, Southeast China. Geol. Mag. 141, 225–231.

Li, X.H., Qi, C.S., Liu, Y., Liang, X.R., Tu, X.L., Xie, L.W., Yang, Y.H., 2005. Petrogenesis of the Neoproterozoic bimodal volcanic rocks along the western margin of the Yangtze Block: new constraints from Hf isotopes and Fe/Mn ratios. Chin. Sci. Bull. 50, 2481–2486.

Li, X.H., Long, W.G., Li, Q.L., Liu, Y., Zheng, Y.F., Yang, Y.H., Chamberlain, K.R., Wan, D.F., Guo, C.H., Wang, X.C., 2010. Penglai zircon megacrysts: a potential new working reference material for microbeam determination of Hf–O isotopes and U–Pb age. Geostand. Geoanal. Res. 34, 117–134.

Li, J.X., Qin, K.Z., Li, G.M., Richards, J.P., Zhao, J.X., Cao, M.J., 2014. Geochronology, geochemistry, and zircon Hf isotopic compositions of Mesozoic intermediate–felsic intrusions in central Tibet: Petrogenetic and tectonic implications. Lithos 198–199, 77–91.

Li, S., Ding, L., Guilmette, C., Fu, J.J., Xu, Q., Yue, Y.H., Henrique-Pinto, R., 2017. The subduction-accretion history of the Bangong-Nujiang Ocean: Constraints from provenance and geochronology of the Mesozoic strata near Gaize, central Tibet. Tectonophysics 702, 42–60.

Li, X.K., Chen, J., Wang, R.C., Li, C., 2018. Temporal and spatial variations of Late Mesozoic granitoids in the SW Qiangtang, Tibet: Implications for crustal architecture, Meso-Tethyan evolution and regional mineralization. Earth Sci. Rev. 185, 374–396.

Li, S., Yin, C., Guilmette, C., Ding, L., Zhang, J., 2019. Birth and demise of the Bangong–Nujiang Tethyan Ocean: A review from the Gerze area of central Tibet. Earth Sci. Rev. 198, 102907.

Liu, T., Zhai, Q.G., Wang, J., Bao, P.S., Qiangba, Z., Tang, S.H., Tang, Y., 2016. Tectonic significance of the Dongqiao ophiolite in the north-central Tibetan plateau: Evidence from zircon dating, petrological, geochemical and Sr–Nd–Hf isotopic characterization. J. Asian Earth Sci. 116, 139–154.

Liu, D.L., Shi, R.D., Ding, L., Huang, Q.S., Zhang, X.R., Yue, Y.H., Zhang, L.Y., 2017. Zircon U–Pb age and Hf isotopic compositions of Mesozoic granitoids in southern Qiangtang, Tibet: Implications for the subduction of the Bangong–Nujiang Tethyan Ocean. Gondw. Res. 41, 157–172.

Ludwig, K.R., 2003. ISOPLOT 3.00: A Geochronological Toolkit for Microsoft Excel. 4. Berkeley Geochronology Center Special Publication, pp. 1–70.

Ma, L., Wang, Q., Kerr, A.C., Yang, J.H., Xia, X.P., Ou, Q., Yang, Z.Y., Sun, P., 2017. Paleocene (c. 62 Ma) leucogranites in southern Lhasa, Tibet: Products of syn-collisional crustal anatexis during slab roll-back? J. Petrol. 58, 2089–2114.

Mahood, G., Hildreth, W., 1983. Large partition coefficients for trace elements in high-silica rhyolites. Geochim. Cosmochim. Acta 47, 11–30.

Maniar, P.D., Piccoli, P.M., 1989. Tectonic discrimination of granitoids. Geol. Soc. Am. Bull. 101, 635–643.

van der Meulen, M.J., Kouwenhoven, T.J., van der Zwaan, G.J., Meulenkamp, J.E., Wortel, M.J.R., 1999. Late Miocene uplift in the Romagnan Apennines and the detachment of subducted lithosphere. Tectonophysics 315, 319–335.

Middlemost, E.A.K., 1994. Naming materials in the magma/igneous rock system. Earth. Sci. Rev. 37, 215–224.

Miyashiro, A., 1974. Volcanic rock series in island arcs and active continental margins. Am. J. Sci. 274, 321–355.

Nabelek, P.I., Liu, M., 2004. Petrologic and thermal constraints on the origin of leucogranites in collisional orogens. Trans. R. Soc. Edinb. Earth Sci. 95, 73–85.

Nocquet, J.M., Sue, C., Walpersdorf, A., Tran, T., Lenôtre, N., Vernant, P., Cushing, M., Jouanne, F., Masson, F., Baize, S., Chéry, J., van der Beek, P.A., 2016. Present-day uplift of the western Alps. Sci. Rep. 6, 28404.

Pan, G.T., Wang, L.Q., Li, R.S., Yuan, S.H., Ji, W.H., Yin, F.G., Zhang, W.P., Wang, B.D., 2012. Tectonic evolution of the Qinghai-Tibet plateau. J. Asian Earth Sci. 53, 3–14.

Peccerillo, A., Taylor, S.R., 1976. Geochemistry of Eocene calc-alkaline volcanic rocks from Kastamonu area, Northern Turkey. Contrib. Miner. Petrol. 58, 63–91.

Petford, N., 2003. Rheology of granitic magmas during ascent and emplacement. Annu. Rev. Earth Planet. Sci. 31, 399–427.

Pitcher, A.S., 1997. The nature and origin of granite. Chapman & Hall, pp. 1–358.

Putirka, K.D., Canchola, J., Rash, J., Smith, O., Torrez, G., Paterson, S.R., Ducea, M.N., 2014. Pluton assembly and the genesis of granitic magmas: Insights from the GIC pluton in cross section, Sierra Nevada Batholith, California. Am. Mineral. 99, 1284–1303.

Qu, X.M., Wang, R.J., Xin, H.B., Jiang, J.H., Chen, H., 2012. Age and petrogenesis of A-type granites in the middle segment of the Bangonghu–Nujiang suture, Tibetan plateau. Lithos 146, 264–275.

Rapp, R.P., Watson, E.B., 1995. Dehydration melting of metabasalt at 8–32 kbar: Implications for continental growth and crust-mantle recycling. J. Petrol. 36, 891–931.

Roberts, M.P., Clemens, J.D., 1993. Origin of high-potassium, calc-alkaline, I-type granitoids. Geology 21, 825–828.

Searle, M., Cottle, J., Streule, M., Waters, D., 2009. Crustal melt granites and migmatites along the Himalaya: melt source, segregation, transport and granite emplacement mechanisms. Earth Environ. Sci. Trans. R. Soc. Edinb. 100, 219–233.

Sisson, T.W., Ratajeski, K., Hankins, W.B., Glazner, A.F., 2005. Voluminous granitic magmas from common basaltic sources. Contrib. Miner. Petrol. 148, 635–661.

Springer, W., Seck, H.A., 1997. Partial fusion of basic granulites at 5–15 kbar: implications for the origin of TTG magmas. Contrib. Mineral. Petrol. 127, 30–45.

Sui, Q.L., Wang, Q., Zhu, D.C., Zhao, Z.D., Chen, Y., Santosh, M., Hu, Z.C., Yuan, H.L., Mo, X.X., 2013. Compositional diversity of ca. 110 Ma magmatism in the northern Lhasa Terrane, Tibet: Implications for the magmatic origin and crustal growth in a continent–continent collision zone. Lithos 168–169, 144–159.

Sun, S.S., Mcdonough, W.F., 1989. Chemical and isotopic systematics of oceanic basalts: implications for mantle composition and processes. Geol. Soc. Lond. Spec. Publ. 42, 313–345.

Tang, Y., Zhai, Q.G., Hu, P.Y., Xiao, X.C., Wang, H.T., Wang, W., Zhu, Z.C., Wu, H., 2019. Jurassic high-Mg andesitic rocks in the middle part of the Bangong-Nujiang suture zone, Tibet: New constraints for the tectonic evolution of the Meso-Tethys Ocean. Acta Petrol. Sin. 35, 3097–3114.

Topuz, G., Altherr, R., Siebel, W., Schwarz, W.H., Zack, T., Hasözbek, A., Barth, M., Satır, M., Şen, C., 2010. Carboniferous high-potassium I-type granitoid magmatism in the Eastern Pontides: the Gümüşhane pluton (NE Turkey). Lithos 116, 92–110.

Vervoort, J.D., Patchett, P.J., Blichert-Toft, J., Albarède, F., 1999. Relationships between Lu–Hf and Sm–Nd isotopic systems in the global sedimentary system. Earth Planet. Sci. Lett. 168, 79–99.

Vervoort, J.D., Plank, T., Prytulak, J., 2011. The Hf–Nd isotopic composition of marine sediments. Geochim. Cosmochim. Acta 75, 5903–5926.

Wang, Q., Zhu, D.C., Cawood, P.A., Zhao, Z.D., Liu, S.A., Chung, S.L., Zhang, L.L., Liu, D., Zheng, Y.C., Dai, J.G., 2015. Eocene magmatic processes and crustal thickening in southern Tibet: Insights from strongly fractionated ca. 43 Ma granites in the western Gangdese Batholith. Lithos 239, 128–141.

Wang, B.D., Wang, L.Q., Chung, S.L., Chen, J.L., Yin, F.G., Liu, H., Li, X.B., Chen, L.K., 2016. Evolution of the Bangong–Nujiang Tethyan ocean: Insights from the geochronology and geochemistry of mafic rocks within ophiolites. Lithos 245, 18–33.

Whalen, J.B., Currie, K.L., Chappell, B.W., 1987. A-type granites: geochemical characteristics, discrimination and petrogenesis. Contrib. Miner. Petrol. 95, 407–419.

Whalen, J.B., McNicoll, V.J., van Staal, C.R., Lissenberg, C.J., Longstaffe, F.J., Jenner, G.A., van Breeman, O., 2006. Spatial, temporal and geochemical characteristics of Silurian collision-zone magmatism, Newfoundland Appalachians: An example of a rapidly evolving magmatic system related to slab break-off. Lithos 89, 377–404.

Wu, F.Y., Sun, D.Y., Li, H., Jahn, B.M., Wilde, S., 2002. A-type granites in northeastern China: age and geochemical constraints on their petrogenesis. Chem. Geol. 187, 143–173.

Wu, F.Y., Jahn, B.M., Wilde, S.A., Lo, C.H., Yui, T.F., Lin, Q., Ge, W.C., Sun, D.Y., 2003. Highly fractionated I-type granites in NE China (I): geochronology and petrogenesis. Lithos 66, 241–273.

Wu, F., Liu, X., Ji, W., Wang, J., Yang, L., 2017. Highly fractionated granites: Recognition and research. Sci. China Earth Sci. 60, 1201–1219.

Wu, F.Y., Liu, X.C., Liu, Z.C., Wang, R.C., Xie, L., Wang, J.M., Ji, W.Q., Yang, L., Liu, C., Khanal, G.P., He, S.X., 2020. Highly fractionated Himalayan leucogranites and associated rare-metal mineralization. Lithos 352–353, 105319.

Xie, L.W., Zhang, Y.B., Zhang, H.H., Sun, J.F., Wu, F.Y., 2008. In situ simultaneous determination of trace elements, U-Pb and Lu-Hf isotopes in zircon and baddeleyite. Chin. Sci. Bull. 53, 1565–1573.

Yang, Z.Y., Wang, Q., Zhang, C.F., Yang, J.H., Ma, L., Wang, J., Sun, P., Qi, Y., 2019. Cretaceous (~100 Ma) high-silica granites in the Gajin area, Central Tibet: Petrogenesis and implications for collision between the Lhasa and Qiangtang Terranes. Lithos 324–325, 402–417.

Yi, J.K., Wang, Q., Zhu, D.C., Li, S.M., Liu, S.A., Wang, R., Zhang, L.L., Zhao, Z.D., 2018. Westward-younging high-Mg adakitic magmatism in central Tibet: Record of a westward-migrating lithospheric foundering beneath the Lhasa–Qiangtang collision zone during the Late Cretaceous. Lithos 316–317, 92–103.

Yin, A., Harrison, T.M., 2000. Geologic evolution of the Himalayan-Tibetan orogen. Annu. Rev. Earth Planet. Sci. 28, 211–280.

Yurimoto, H., Duke, E.F., Papike, J.J., Shearer, C.K., 1990. Are discontinuous chondrite-normalized REE patterns in pegmatitic granite systems the results of monazite fractionation? Geochim. Cosmochim. Acta 54, 2141–2145.

Zeng, L.S., Gao, L.E., 2017. Cenozoic crustal anatexis and the leucogranites in the Himalayan collisional orogenic belt. Acta Petrol. Sin. 33, 1420–1444.

Zeng, Y.C., Chen, J.L., Xu, J.F., Wang, B.D., Huang, F., 2016. Sediment melting during subduction initiation: Geochronological and geochemical evidence from the Darutso high-Mg andesites within ophiolite melange, central Tibet. Geochem. Geophys. Geosyst. 17, 4859–4877.

Zhang, K.J., Zhang, Y.X., Tang, X.C., Xia, B., 2012. Late Mesozoic tectonic evolution and growth of the Tibetan plateau prior to the Indo-Asian collision. Earth Sci. Rev. 14, 236–249.

Zhang, X., Shi, R., Huang, Q., Liu, D., Gong, X., Chen, S., Yi, G., Wu, K., Sun, Y., Ding, L., 2014. Early Jurassic high-pressure metamorphism of the Amdo terrane, Tibet: Constraints from zircon U–Pb geochronology of mafic granulites. Gondw. Res. 26, 975–985.

Zhang, L., Ren, Z.Y., Xia, X.P., Li, J., Zhang, Z.F., 2015. IsotopeMaker: A Matlab program for isotopic data reduction. Int. J. Mass Spectr. 392, 118–124.

Zhang, Q., Wang, Q., Li, G., Cui, X., 2018. Fractionation process of high-silica magmas through the lens of zircon crystallization: A case study from the Tengchong Block, SW China. Chem. Geol. 496, 34–42.

Zhong, Y., Liu, W.L., Xia, B., Liu, J.N., Guan, Y., Yin, Z.X., Huang, Q.T., 2017. Geochemistry and geochronology of the Mesozoic Lanong ophiolitic mélange, northern Tibet: Implications for petrogenesis and tectonic evolution. Lithos 292, 111–131.

Zhu, D.C., Zhao, Z.D., Niu, Y., Mo, X.X., Chung, S.L., Hou, Z.Q., 2011. The Lhasa Terrane: record of a microcontinent and its histories of drift and growth. Earth Planet. Sci. Lett. 301, 241–255.

Zhu, D.C., Zhao, Z.D., Niu, Y.L., Dilek, Y., Hou, Z.Q., Mo, X.X., 2013. The origin and pre- Cenozoic evolution of the Tibetan Plateau. Gondw. Res. 23, 1429–1454.

Zhu, D.C., Wang, Q., Zhao, Z.D., Chung, S.L., Cawood, P.A., Niu, Y.L., Liu, S.A., Wu, F.Y., Mo, X.X., 2015. Magmatic record of India-Asia collision. Scientific Reports 5, 14289.

Zhu, D.C., Li, S.M., Cawood, P.A., Wang, Q., Zhao, Z.D., Liu, S.A., Wang, L.Q., 2016. Assembly of the Lhasa and Qiangtang terranes in central Tibet by divergent double subduction. Lithos 245, 7–17.

Zhu, Z., Zhai, Q., Hu, P., Chung, S., Tang, Y., Wang, H., Wu, H., Wang, W., Huang, Z., Lee, H., 2019. Closure of the Bangong–Nujiang Tethyan Ocean in the central Tibet: Results from the provenance of the Duoni Formation. J. Sediment. Res. 89, 1039–1054.